Full length article

Photothermocatalytic performance of ACo$_2$O$_4$ type spinel with light-enhanced mobilizable active oxygen species for toluene oxidation

Xi Chen[a,b], Songcai Cai[a,b], Enqi Yu[a,b], Juanjuan Li[a], Jing Chen[b,c,d], Hongpeng Jia[a,b,*]

[a] CAS Center for Excellence in Regional Atmospheric Environment, and Key Laboratory of Urban Pollutant Conversion, Institute of Urban Environment, Chinese Academy of Sciences, Xiamen 361021, China
[b] University of Chinese Academy of Sciences, Beijing 100049, China
[c] Xiamen Institute of Rare-earth Materials, Haixi Institutes, Chinese Academy of Sciences, Xiamen 361021, China
[d] Fujian Institute of Research on the Structure of Mater, Chinese Academy of Sciences, Fuzhou 350002, China

ARTICLE INFO

ABSTRACT

Recently, photo-thermocatalysis has been intensively motivated since it is beneficial for both relieving energy consumption and using the full solar spectrum energy. In this work, efficient photo-promoted thermocatalytic removal of VOCs has been investigated on ACo$_2$O$_4$ (A = Ni, Cu, Fe, Mn) spinel by harvesting inexhaustible solar energy to provide thermal energy. ACo$_2$O$_4$ was synthesized by co-precipitation method, which exhibits strong light absorption in the entire solar spectrum (200–2500 nm) and high solar heating effect, providing enough thermal energy for catalytic degradation of toluene. The photo-thermocatalytic performance of ACo$_2$O$_4$ catalysts follows the sequence: NiCo$_2$O$_4$ > CuCo$_2$O$_4$ > FeCo$_2$O$_4$ > MnCo$_2$O$_4$, in which NiCo$_2$O$_4$ exhibits the highest photo-thermocatalytic activity (93% for toluene conversion and 80% for CO$_2$ yield) and good stability (at least for 20 h) for toluene oxidation under irradiation. And such excellent light-driven catalytic performance over NiCo$_2$O$_4$ can be mainly explained by its strong light absorption, high photo-thermal conversion, more active oxygen species, enlarged surface area and the better OCS. Besides, a novel light-enhanced effect is revealed to considerably increase the photo-thermocatalytic activity for toluene oxidation, which is quite different from the traditional photocatalysis. By combining CO temperature-programmed reduction (CO-TPR) and *in situ* diffuse reflectance infrared Fourier transform spectroscopy (*in situ* DRIFTS), it is revealed that the irradiation is able to enhance the mobility of active oxygen species, resulting in a significant improvement of photo-thermocatalytic activity over NiCo$_2$O$_4$.

1. Introduction

Volatile organic compounds (VOCs), as one kind of important precursors of photochemical smog and ozone, lead to a diverse range of environmental problems [1]. Over the past decades, various control technologies have been used in the removal of VOCs, such as catalytic oxidation [2], plasma technology [3], photocatalytic oxidation [4] and so on. Among them, photocatalysis is regarded as a clean and economical approach to degrade VOCs by using clean solar energy. However, traditional photocatalysis merely uses the part of sunlight like ultraviolet light and visible light, which only accounts for approximately 47% of whole solar spectrum [5,6]. It means that the rest around 50% of sun energy is wasted. In order to promote the use efficiency of sun energy, considerable research efforts have been devoted to developing novel materials with broad photo-response to take full

advantages of sunlight for decades [7]. Recently, using the full spectrum light as an efficient thermal source to drive catalytic reactions have been reported such as photo-thermocatalytic NO oxidation and benzene decomposition [8,9], which fully utilizes the strong heating effect of light especial for IR light.

Cobalt oxides have been widely applied in fields of environmental pollutants degradation and photoreduction of CO$_2$ [10,11]. For VOCs photodegradation, its photocatalytic capacity is primarily restricted by its low oxidation potential of the photogenerated holes (h$_{CB}^+$) [12], which is inadequate to the direct oxidation of VOCs with high potential (such as toluene) [13]. As an efficient thermocatalytic catalyst, Co$_3$O$_4$, featuring polyvalence and polymorphism, has exhibited high efficiency for the abatement of multiple gaseous contaminants (CO, NO$_x$, and VOCs) [14–16]. However, it is required to drive this process by an external heat such as thermocatalytic removal of recalcitrant VOCs

---

pollutants, which results in a high nonrenewable energy consumption. In view of the excellent light absorption capacity of Co_3O_4 and the strong thermal heating effect of IR light [17,18], the employment of solar thermal energy to supply enough external heat to drive catalytic process over Co_3O_4 seems to be an ideal strategy to increase the total solar energy utilization efficiency and save energy. For realizing efficient solar-driven thermocatalytic oxidation, it is highly desired to design catalysts with high thermocatalytic activity and strong light absorption over whole solar spectrum.

Recently, defect engineering is extensively used to regulate the catalytic activity of metal oxides [19–21]. Secondary metal doping is an effective method to enhance the concentration of defects existed in catalyst, such as oxygen vacancy or lattice defect, which supply more active sites and active oxygen species, and further promote the catalytic removal of VOCs [22,23]. Besides, the light absorption capacity of material can be modulated by secondary metal doping [24]. Thus, doping the appropriate metal into Co_3O_4 seems to be feasible to obtain catalyst with more defects and simultaneous realize efficient solar-utilization to drive thermocatalytic oxidation of VOCs. Herein, a series of ACo_2O_4 (A = Ni, Cu, Fe, Mn) spinels with strong light absorption over the whole solar spectrum was synthesized through a simple co-precipitation method. Among them, Ni doped spinel ($NiCo_2O_4$) exhibits the highest photo-thermocatalytic activity (93% of toluene conversion and 80% of CO_2 yield) and good stability (at least for 10 cycles and each cycle for 2 h) for toluene oxidation under irradiation (400 mW/cm²). The investigation of catalyst physicochemical properties reveals that doping with appropriate metal can not only improve the light absorption capacity but also activate more surface oxygen species, which lead to an enhanced catalytic performance for toluene degradation. In addition, a light-enhanced effect was found to be able to boost the photo-thermocatalytic activity, which was verified by CO-TPR and *in situ* DRIFTS analysis.

2. Experimental section

2.1. Materials

All chemicals (A.R. grade) were purchased from Sinopharm Chemical Reagent Co., Ltd., including nickel (II) nitrate hexahydrate ($Ni(NO_3)_2·6H_2O$), copper (II) nitrate tirhydrate ($Cu(NO_3)_2·3H_2O$), manganese (II) nitrate ($Mn(NO_3)_2$, 50 wt% aqueous solution), iron (III) nitrate nonahydrate ($Fe(NO_3)_3·9H_2O$), cobalt (II) nitrate hexahydrate ($Co(NO_3)_2·6H_2O$), urea, ethanol and toluene.

2.2. Synthesis of catalyst

A simple co-precipitation method was used to synthesize ACo_2O_4 type spinel. Typically, 0.58 g (2 mmol) $Ni(NO_3)_2·6H_2O$, 1.75 g (4 mmol) $Co(NO_3)_2·6H_2O$, 1.08 g (18 mmol) urea and 60 mL deionized water were mixed and then stirred for 20 min at room temperature. The obtained solution was transferred to a 100 mL Teflon-lined stainless-steel autoclave. The reactor was sealed and heated at 120 °C for 6 h. Subsequently, the solid was filtered and washed with water/ethanol for several times, and then dried at 80 °C overnight. Finally, the $NiCo_2O_4$ was obtained by calcination at 300 °C for 3 h in air flow. The similar procedure was employed to prepare $FeCo_2O_4$, $MnCo_2O_4$ and $CuCo_2O_4$ spinel by using $Fe(NO_3)_3·9H_2O$, $Mn(NO_3)_2$ solution, and $Cu(NO_3)_2·3H_2O$ to instead of nickel salt, respectively.

As a reference compound, Co_3O_4 was prepared by the similar procedure mentioned above except that the $Co(NO_3)_2·6H_2O$ dosage was increased to 1.75 g (6 mmol).

2.3. Characterization

The X-ray diffraction patterns were obtained by an X'Pert Pro diffractometer using a Cu-Ka radioactive source (40 kV, 40 mA) with a

speed of 12°/min in the 2θ range of 15–90°. Raman spectra were recorded using green laser (532 nm) on a HORIBA spectrometer. The metal contents of catalysts were determined by inductively coupled plasma optical emission spectrometer (ICP-OES). The morphologies of catalysts were studied by using the scanning electronic microscope (SEM, Hitachi S-4800). Physisorption instrument (Quantachrome Autosorb IQ) was applied to measure N_2 adsorption-desorption profiles of samples. And specific surface area and pore size distribution were calculated by Brunauer-Emmett-Teller (BET) and Barrett-Joyner-Halenda (BJH) methods, respectively. X-ray photoelectron spectroscopy (XPS) was applied to get insight into the surface chemical states of samples on a Quantum 2000 instrument (ULVAC-PHI). Diffuse reflectance spectra (DRS) of samples in the range of 200–2500 nm were recorded using a Shimadzu UV-2550 spectrophotometer. O_2 temperature-programmed desorption (O_2-TPD) and oxygen storage capacity (OSC) measurements were conducted on a Quantachrome chemisorption instrument. O_2-TPD was carried out as follows: First, the catalyst was preconditioned under 5% O_2/He flow (70 mL/min) at 300 °C for 1 h, then was cooled down to 50 °C; After that, He stream (70 mL/min) was introduced to wipe out the physically absorbed oxygen on the surface of sample for 0.5 h; Finally, the sample was heated up from 50 °C to 800 °C in a gas flow of He (70 mL/min) and the data was collected by a thermal conductivity detector (TCD). The detailed procedure for OSC measurement is described as follows: 50 mg of sample was initially reduced at 200 °C for 45 min by 5% H_2 in Ar (30 mL/min); Then pure He was used to wipe out residual H_2 for 30 min at 200 °C; Subsequently, a 20% O_2/He stream was repeatedly injected into the pre-treated sample until saturation. The consumed oxygen was defined as OSC.

CO temperature-programmed reduction (CO-TPR) of the sample under the full spectrum illumination with auxiliary heating or under direct heating condition was performed on a gas chromatography (GC-9160) furnished with a detector of TCD. Approximate 0.025 g of $NiCo_2O_4$ was put in a cylindrical stainless-steel reactor, and the reaction temperature was recorded by the thermocouple on the surface of catalyst layer. First, the sample was swept with 5% CO/He for 30 min in a flow of 50 mL/min to remove the physically-absorbed oxygen species. Then, the pretreated sample was heated from room temperature to 214 °C with (100 mW/cm²) or without irradiation, and finally maintained at this temperature in the flow of 5% CO/He gas under irradiation or in the dark, respectively.

In situ DRIFTS was analyzed using a FTIR spectrometer (Thermo Fisher is50). Before starting, the sample cell was purged by N_2 for 1 h at ambient temperature, and the spectra of the catalyst were collected as the background. After that, N_2 flow containing 1000 ppm toluene was introduced into reaction cell for 30 min, and then the infrared spectra were continuously collected in the air during the reaction under direct heating at different temperature (170, 190, 210 and 230 °C) or irradiation (400 mW/cm²).

2.4. Catalytic tests

The catalytic degradation of toluene over catalysts was performed under irradiation of full spectrum light (PLS-SXE300UV, PerfectLight) or infrared light (IR lamp, PHILIPS IR 375 W). The light intensity was measured using an optical power meter (CEL-NP2000-2, PerfectLight). And the cut-off filter was used to obtain UV–Vis light or pure infrared light.

The catalytic reaction was performed in a cylindrical stainless-steel reactor, as illustrated in Scheme 1. Approximate 0.025 g of sample was dispersed in 10 mL of absolute ethanol, then spread on a fiberglass-membrane (φ = 25 mm). To reduce the energy loss in the reaction process, an aluminum silicate fiber membrane (φ = 25 mm) was placed under the catalyst bed. The reaction temperature under light irradiation was measured by locating a thermocouple on the center of the catalyst surface. The reaction airstream containing 220 ppm of toluene was
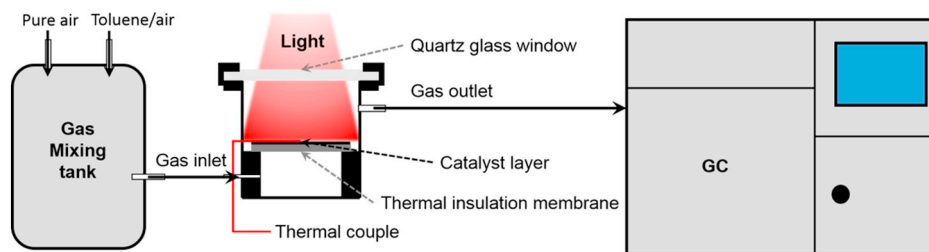
Scheme 1. Schematic diagram of the photothermocatalytic setup.

introduced into the reactor with a gas hourly space velocity (GHSV) of 32,000 mL/g·h. The catalytic efficiency of catalyst was evaluated by monitoring concentration variation of reactant and product using GC-9160 furnished with FID and TCD. During the catalytic reaction, only carbon dioxide as final product was detected, thus toluene conversion and CO_2 yield were determined by the following formulas:

$$\text{Toluene conversion (\%)} = 100 \times ([\text{Toluene}]_{in} - [\text{Toluene}]_{out}/[\text{Toluene}]_{in} \tag{1}$$

$$CO_2 \text{ yield (\%)} = 100 \times [CO_2]_{produced}/[CO_2]_{theoretical} \tag{2}$$

3. Results and discussion

3.1. Characterization of catalysts

As displayed in Fig. 1(a), XRD patterns of all samples show similar peaks that can be well-indexed to that of standard AB_2O_4 spinel from JCPDS cards and other references [25–28]. It confirms that the as-obtained samples belong to the ACo_2O_4 spinel by the co-precipitation method. Element composition analyzed by ICP-OES reveals that the actual molar ratios of Co/A for samples are close to 2:1 (listed in Table 1), which further verify ACo_2O_4 spinel was successfully synthesized. For $MnCo_2O_4$ and $FeCo_2O_4$, it should be noted that some impurity peaks are observed in XRD patterns, which can be attributed to Mn_3O_4 and Fe_2O_3 phases, respectively. This indicates some Mn and Fe element are not doped into the crystal lattice of spinel and are separated out to form oxides under calcination. However, no impure phases can be observed for $NiCo_2O_4$ and $CuCo_2O_4$ samples, which implies the Ni and Cu element are doped into Co_3O_4 structure successfully, forming the uniform ACo_2O_4 structures. Compared to pure Co_3O_4, all peaks of samples are broadened and weakened, which is possibly due to the destruction of long-range ordered structure in samples by doping the secondary metal ions [23]. Generally, the accumulation of long-rang disorder in structure can facilitate more vacancies or defects, which are believed to

be favor to oxidative degradation of VOCs [23,29].

The structure of samples was further studied by Raman spectra. As shown in Fig. 1(b), pure Co_3O_4 evidently presents four strong peaks at around 194, 480, 518 and 687 cm^{-1}, corresponding to the modes (A_{1g}, E_g and 2 F_{2g}) of a crystalline Co_3O_4 spinel [30]. The strongest peak around 687 cm^{-1} corresponding to A_{1g} symmetry is attributed to the vibration from the octahedral sites (CoO_6) of the spinel Co_3O_4, which is susceptible to structural change such as lattice defect [18,31]. After doping of secondary metal, the obvious change of Raman peaks can be observed, where the change difference mainly depended on the doped metal ions. As observed, the A_{1g} band slightly shift to lower frequency from 687 cm^{-1} (Co_3O_4) to 684 cm^{-1} ($FeCo_2O_4$), 683 cm^{-1} ($MnCo_2O_4$), 681 cm^{-1} ($CuCo_2O_4$) and 655 cm^{-1} ($NiCo_2O_4$), respectively, with gradual broadening and fading. Synchronously, the E_g (480 cm^{-1}) and F_{2g} (518 cm^{-1}) bands of samples are weakened and broadened. Especially for $NiCo_2O_4$, a very broader Raman peak is shaped by integrating A_{1g}, E_g and F_{2g} band. These phenomena can be interpreted that metal doping results in the occurrence of structure disorder and form more lattice defects by lattice deformation [32]. It is mutually echoed for XRD and Raman analysis, thus structure disorder by metal doping is beneficial for toluene oxidation [29]. Additionally, no obvious peaks for AO_x (A = Ni, Cu) appear, which imply the doped metal is highly dispersed in ACo_2O_4 (A = Ni, Cu). By zooming the Raman spectra of $MnCo_2O_4$ and $FeCo_2O_4$, the characteristic peak with low intensity

Table 1
Element composition and physical properties of samples.

Samples	S_{BET} (m^2/g)	Average pore size (nm)	Co:A molar ratios by ICP-OES	Absorptance (a, %)
Co_3O_4	57.9	15.19	–	94.78
$NiCo_2O_4$	115.0	11.64	Co:Ni = 2.08:1	99.13
$CuCo_2O_4$	97.4	9.96	Co:Cu = 2.07:1	97.56
$FeCo_2O_4$	93.1	19.76	Co:Fe = 2.05:1	95.32
$MnCo_2O_4$	77.4	7.01	Co:Mn = 2.05:1	95.16

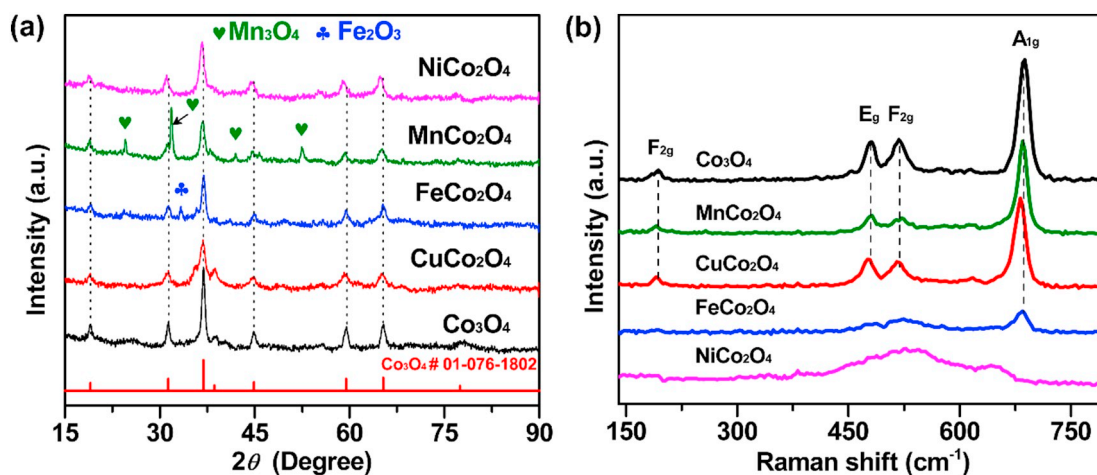**Fig. 1.** XRD patterns (a) and Raman spectra (b) of samples.
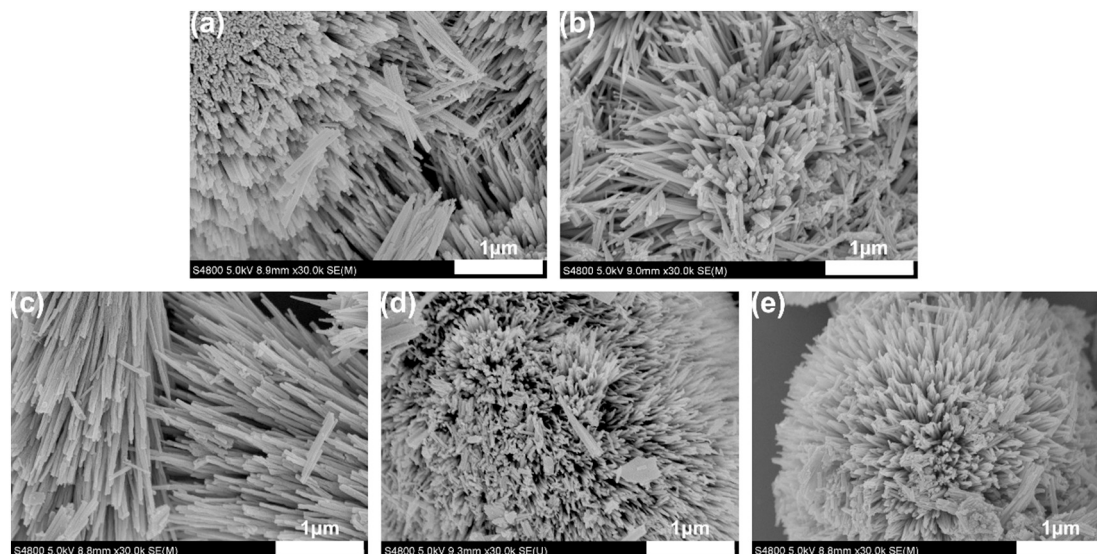
Fig. 2. SEM images of Co_3O_4 (a), $NiCo_2O_4$ (b), $CuCo_2O_4$ (c), $FeCo_2O_4$ (d), $MnCo_2O_4$ (e).

which belongs to Fe_2O_3 ($504\,cm^{-1}$) and Mn_3O_4 ($650\,cm^{-1}$) can be observed [33,34], confirming the existence of small amount of Fe_2O_3 and Mn_3O_4 species in $FeCo_2O_4$ and $MnCo_2O_4$ sample, respectively. And it is consistent with XRD measurement.

The SEM can be used to intuitively examine the morphologies of prepared spinel samples. As displayed in Fig. 2, the similar morphologies are observed for all samples, composing of stacked needle-shaped oxides. It is helpful to form stacking porous structure that can accelerate diffusion of reactant molecule and provide more active sites [35]. The porous structure of all samples has also been investigated by N_2 adsorption-desorption isotherm and pore-size distribution (Fig. S2). The isotherms of all samples are identified as type V with the hysteresis loops demarcated between type H3 and H4 loops, which confirm presence of irregular mesoporous structure. The S_{BET} and average pore size of samples were calculated and listed in Table 1. Compared to pure Co_3O_4, after introduction of secondary metal ions, the S_{BET} of ACo_2O_4 are obviously enlarged. The largest value of S_{BET} is 115 m^2/g for Ni Co_2O_4, which is around two times as much as Co_3O_4 (57.9 m^2/g). Distribution of pore diameter indicates that the mesoporous mainly exist in ACo_2O_4. It is generally accepted that the higher specific surface area is conducive to VOCs oxidation due to exposure of more active sites [36].

The UV–Vis DRS measurement is adopted to estimate the optical properties of samples. All samples display strong light absorption over the entire spectral range (200–2500 nm), suggesting they could be ideal light absorber materials. For Co_3O_4, the two obvious absorption regions are showed in Fig. 3. The band of 330–800 nm is from the Co^{2+}–O^{2-} charge transfer, the metal-to-metal charge transfer (MMCT) effect of Co^{3+}-Co^{2+} and the low-spin Co^{3+}, and the band of 1100–1850 nm is attributed to the high-spin Co^{2+} and the MMCT effect of Co^{3+}-Co^{2+} [11]. After metal doping, it results in the different enhanced capacity for light absorption, as dispatched in Fig. 3. The difference is rooted in the MMCT effect between Co ions and A ions, which is susceptible to the d-d indirect transition bandgap of A ions [18]. In pure Co_3O_4, the charge transfer occurs directly from valence band (VB) to conduction band (CB). when the doped metal ions exist in ACo_2O_4, the excited electrons are not transferred from VB to CB and they can be captured by the unoccupied A ions, thus altering the light absorption of material [37]. Due to the different transition of A ions, it leads to the different optical response in some regions [38]. For $NiCo_2O_4$ and $zCuCo_2O_4$ samples, the spectra display significant enhancement in the entire region compared to that of pure Co_3O_4, which imply the introduction of Ni and Cu ions can improve the charge transition of samples. However,
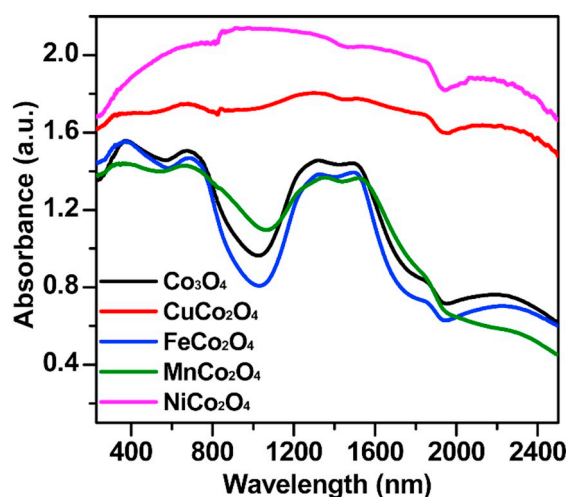

Fig. 3. UV–vis DRS spectra of the samples.

the Mn and Fe doping can not enhance the light absorbance and even lower light absorbance in some regions. Therefore, it is difficult to accurately estimate whether the light-absorption capacity of material is enhanced by the addition of secondary metal ions. For further comprehension about how the optical property of material responds to the introduction of secondary metal, we calculated the absorption coefficient (a) by the equation as follows:

$$a\,(\%) = \left(\int (1 - R\,(\lambda)) * E_{sol} \right) / \int E_{sol}\ (230 \le \lambda \le 2500\ nm) \tag{3}$$

where the E_{sol} is the solar radiation power at AM 1.5 and $R\,(\lambda)$ is the spectral reflectance from Fig. S3.

The a value of samples was listed as follows the sequence: $NiCo_2O_4 > CuCo_2O_4 > FeCo_2O_4 > MnCo_2O_4 > Co_3O_4$ (Table 1). It is worth mentioning that the absorption coefficient of samples is not well agreement with DRS absorbance profile, which is because that the absorption coefficient was calculated by the light reflectance of sample. All ACo_2O_4 samples show enhanced absorption efficiency as compared to Co_3O_4, ascribed to the damping effect of A ion d-d transitions. The d-d indirect bandgap of Ni ion is 3.4 eV for NiO, which is much higher than other ions (Mn-1.7 eV, Fe-2.0 eV, Cu-1.9 eV and Co-1.6 eV), leading to the strongest optical absorption of $NiCo_2O_4$ [39–43]. The a value of $NiCo_2O_4$ is notably raised up to 99%, which indicates the
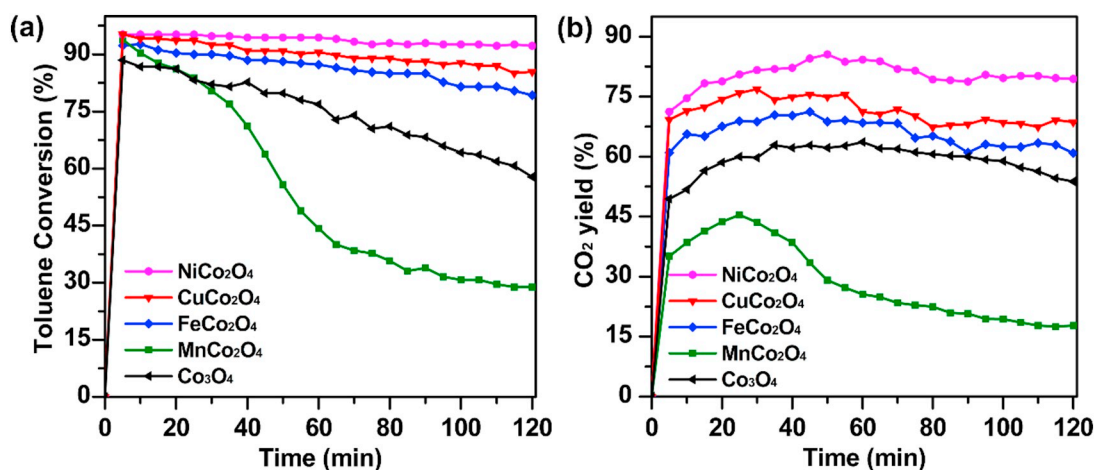
Fig. 4. Toluene conversion (a) and CO_2 yield (b) over the catalysts under the irradiation (simulated sunlight, $400\,mW/cm^2$).

$NiCo_2O_4$ can be applied to absorb radiation at all angles efficiently and release thermal energy by converting absorbed photons (photo-to-thermal conversion), leading to enough energy to drive a target reaction (such as toluene oxidation).

3.2. Catalytic behavior of materials

To confirm the capacity to drive reaction on the as-prepared Co-based catalysts, the catalytic performance for toluene oxidation was carried out. As shown in Fig. 4, the Co_3O_4 catalyst exhibits a moderate catalytic performance for toluene oxidation. Upon irradiation, toluene conversion quickly reaches to 90% at the beginning and then is slowly reduced to 60% in 120 min, and CO_2 yield is floated around 50%–60% with reaction time. The decreasing of conversion is possibly due to the coverage of active sites by accumulated intermediates. After the doping of secondary metal element, it leads to the totally different effects on the catalytic activity of sample. The $MnCo_2O_4$ exhibits a decreased catalytic performance while the catalytic activities of $NiCo_2O_4$, $CuCo_2O_4$ and $FeCo_2O_4$ are apparently enhanced at least for 120 min. As expected, $NiCo_2O_4$ displays the better stability and higher catalytic activity (toluene conversion of 93% and CO_2 yield of 80%) within 120 min, which is possibly related to its preeminent light absorption capacity. The light absorption results in the increase of temperature on catalyst layer by converting photons to fulfill the photothermal effect, which provides enough energy to trigger catalytic oxidation of toluene. The conversion of thermal energy was evaluated by surface temperature evolution profiles on catalyst layer (Fig. S4). The surface temperatures of all samples can be quickly raised to $> 200\,°C$ and then slowly reach to the stable state, where the energy absorption and dissipation build up a balance. The equilibrium temperature on catalyst surface follows the sequence: $NiCo_2O_4 > CuCo_2O_4 > FeCo_2O_4 > MnCo_2O_4 > Co_3O_4$, which well matches with the data of absorption coefficient. Compared to blank membrane, the surface temperature on catalyst layer is much higher due to the strong photo-thermal conversion on catalysts. Further investigation for the efficiency of photo-thermal conversion (η) is performed, as shown in Fig. S5. The photothermal conversion efficiencies of Co_3O_4, $NiCo_2O_4$, $CuCo_2O_4$, $MnCo_2O_4$ and $FeCo_2O_4$ are calculated to be 5%, 6.7%, 7.6%, 7.8% and 7.9%, respectively. This result indicates that the introduction of secondary metal can promote the photothermal conversion efficiency of Co_3O_4.

Furthermore, it is also noted that the catalytic activity of catalyst for toluene degradation is largely influenced by light intensity. As shown in Fig. 5(a) and (b), the catalytic performance on $NiCo_2O_4$ is positively related to light intensity. When the light intensity is $400\,mW/cm^2$, the conversion and mineralization over $NiCo_2O_4$ are more stable and exhibit the best performance within 120 min. With decreasing of light intensities from 400 to $100\,mW/cm^2$, the catalytic performance is

obviously decreased. Synchronously, the monitoring of surface temperature on catalyst layer confirms that the variation of temperature is completely depended on light intensity, giving 214, 199, 171, 129, $70\,°C$ corresponding to 400, 350, 300, 200, $100\,mW/cm^2$, respectively. In other words, the difference in catalytic activity is caused by different surface temperature of catalyst that is determined by incident light intensity. Thus, its catalytic behavior for toluene oxidation is more likely suitable for thermocatalysis, in which the required thermal energy is from light conversion.

To further reveal whether the catalytic performance of Co-based catalyst under irradiation possibly comes from traditional photocatalytic process, we conducted the toluene oxidation on the catalysts at low temperature (Fig. S6). It was found that neither toluene conversion nor CO_2 was obviously detected for all the samples under irradiation at low-temperature (38–49 °C, controlled by ice-bath). This implies the Co-based catalyst in this work is totally inert for photocatalytic degradation of toluene, which can be ascribed that the low redox potential nature of Co-based catalyst (< 2.44 vs. NHE) is deficient for toluene oxidation with high redox potential (2.61 vs. NHE) [11,44]. Instead of reacting with oxidative species as the traditional photocatalysis, the photo-generated charge carrier on the catalyst is recombined by a nonradiative recombination process, leading to an efficient photothermal conversion [45].

In view of the $NiCo_2O_4$ presents a high light absorption efficiency across the entire solar spectrum region, it is highly necessary to investigate which region made the most important contribution to the catalytic activity under illumination. The control of light intensity and temperature by irradiation are applied to catalytic performance of toluene degradation on $NiCo_2O_4$. As displayed in Fig. 6, the catalytic behavior of $NiCo_2O_4$ under different light irradiation with same light intensity exhibits the order of results as follows: UV–vis SL (189 °C) < UV–vis-IR (214 °C) < IR SL (235 °C), which is in accordance with the surface temperature of catalyst layer. It implies that the temperature plays a key role in the photo-thermal catalysis and the IR light has a strong contribution to heating effect. In addition, to study the influence on catalytic activity by photon energy from different light, the catalytic performance on $NiCo_2O_4$ was carried out by tuning light intensity of UV–vis-IR, UV–vis and IR light to maintain the surface temperature of catalyst layer at 214 °C. The sequence of catalytic activity is IR ST ($288\,mW/cm^2$) < UV–vis-IR ($400\,mW/cm^2$) < UV–vis ST ($530\,mW/cm^2$), which reveals that high photon energy (UV–Vis) is helpful to promote toluene oxidation at the same temperature. As mentioned above, no traditional photocatalysis is involved in the reaction, therefore, it indicates that toluene oxidation on $NiCo_2O_4$ under irradiation is a predominant light-driven thermocatalysis accompanying with additional contribution of UV–vis light. To further verify
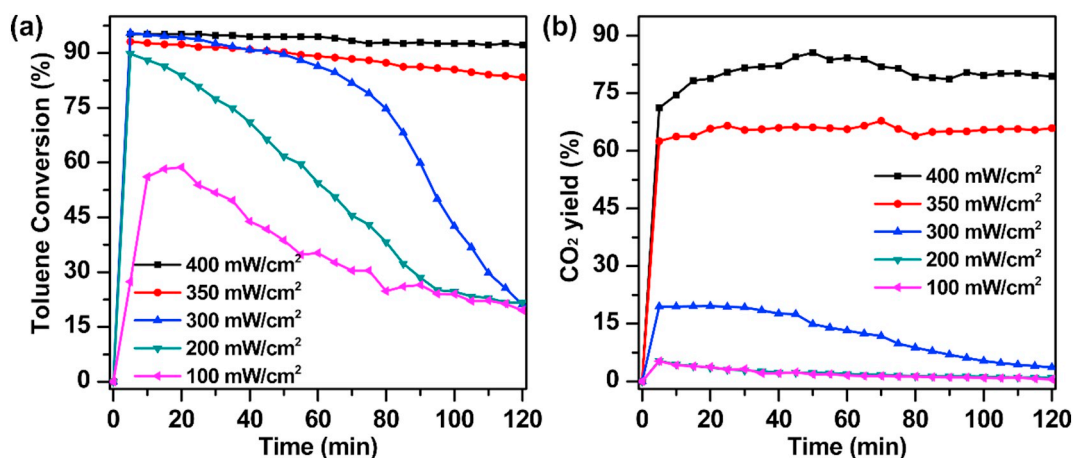
Fig. 5. Toluene conversion (a) and CO_2 yield (b) over $NiCo_2O_4$ under irradiation of simulated sunlight with different intensities.
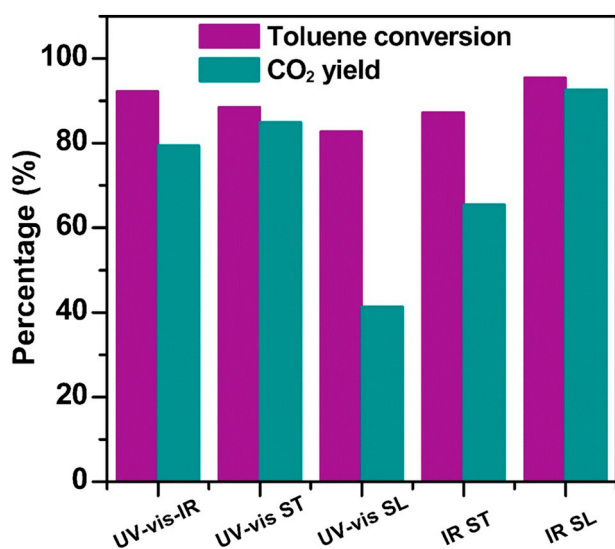

Fig. 6. Toluene conversion and CO_2 yield of $NiCo_2O_4$ under the irradiation of simulated sunlight, UV–vis, and infrared with the same light intensity of 400 mW/cm^2 (SL) or at the same temperature at 214 °C (ST).

the existence of the additional contribution of light, the toluene degradation behavior over these catalysts under heating condition was investigated as a comparison (Fig. S7). Remarkably, the catalytic performance over the Co-based catalysts under the irradiation condition is higher than that under heating condition, which also confirms that the light has additional effects in the photo-thermocatalytic process.

3.3. Origin of catalytic activity

As we know, catalytic activity for toluene oxidation is closely associated with components and oxygen species of the catalyst [46]. Thus, it is necessary to get a general understanding for surface species and chemical states of catalyst by XPS analysis (Fig. 7). The XPS spectra of Co 2p shows two deconvoluted peaks located at 779.6 and 780.9 eV, ascribed to Co^{3+} and Co^{2+} ions, respectively [18]. For O1s spectra, the three deconvoluted peaks at 532.6, 531.0 and 529.6 eV are attributed to adsorbed water (O_{H2O}), adsorbed oxygen (O_{ads}) and surface lattice oxygen (O_{latt}) [47,48]. The ratios of Co^{3+}/Co^{2+} and O_{ads}/O_{latt} are calculated and listed in Table 2. There is no significant change for Co^{3+}/Co^{2+} ratio, implying it is not the main factor to influence the catalytic activity of ACo_2O_4 compared to that of Co_3O_4. However, the ratio of O_{ads}/O_{latt} is totally different according to the doped metal ions. It obeys the order as $NiCo_2O_4 > CuCo_2O_4 = FeCo_2O_4 > Co_3O_4 > MnCo_2O_4$, which is

consistent with their catalytic activities. This result points out that the surface adsorbed oxygen plays a leading role in the photo-thermocatalytic reaction. In addition, it is worth to note that the deconvoluted peaks of lattice oxygen are apparently shifted toward a lower binding energy compared to that in Co_3O_4, which reveals there are more surface oxygen vacancies in the sample. The existed oxygen vacancies lead to redistribution of positive charge on the residual oxygen ions, thus resulting in lower binding energy for O 1s [49]. Besides, the secondary metal in low state (Cu^+, Fe^{2+}, Mn^{3+}, Ni^{2+}) was found in the XPS spectra (Fig. 7(c)), and it also implies the presence of oxygen vacancies. Therefore, the variation of surface O_{ads} is mainly induced by the existence of oxygen vacancy, which is caused by the addition of secondary metals. Owing to the electronegativity nature of oxygen vacancy, the catalyst is able to activate detached O species (monatomic O, O_2^{2-} and O^-) from atmosphere, leading to the accumulation of O_{ads} on its surface.

The chemical absorption ability of oxygen in samples by oxygen vacancies is identified by oxygen storage capacity (OSC) measurement. As listed in Table 2, OSC value of Co_3O_4 (833 µmol/g) is more than that of $MnCo_2O_4$ (563 µmol/g) and $FeCo_2O_4$ (761 µmol/g), but is lower than that of $NiCo_2O_4$ (1667 µmol/g) and $CuCo_2O_4$ (2896 µmol/g). It implies the addition of Ni and Cu ions is helpful to produce more oxygen defects for the activation of oxygen. Combined with XPS spectra of O1s, the introduction of Ni leads to more defects on the surface of material that can create more effective surface O_{ads} species although $CuCo_2O_4$ owns the highest value of OSC [50,51].

To get insight into the activation of active oxygen species and oxygen mobility, O_2-TPD of the catalyst was carried out. Generally, the desorption of oxygen species obeys the sequence $O_2 (ad) \rightarrow O_2^- (ad) \rightarrow O^- (ad) \rightarrow O^{2-}$ (lattice) with increasing of temperature [52]. The $O_2 (ad)$ is ascribed as physically adsorbed oxygen, which can be easily eliminated by the pretreatment of He flow. The O_2^- and O^- species belongs to the chemical adsorbed oxygen are located at surface vacancies and it can be detached at low-temperature region (100 °C-400 °C) [53]. O^{2-} (lattice) refers to the lattice oxygen, which is hard to desorb. As shown in Fig. 8, the strong and broad peaks around 450–800 °C are attributed to the extraction of surface and bulk lattice oxygen. Impressively, a very strong O^{2-} (lattice) peak is observed at low temperature for $MnCo_2O_4$ compared to Co_3O_4 and other ACo_2O_4 samples, which demonstrates that the addition of Mn results in more lattice oxygen and enhances the low-temperature mobility of lattice oxygen. It is also verified for analysis of XPS, where the $MnCo_2O_4$ exhibits the highest ratio of O_{latt}/O_{ads} even higher than Co_3O_4. Considering the actual catalytic reaction in the experiments occurs below 210 °C, thus the desorption behavior of oxygen species on catalysts at low temperature is mainly investigated. As displayed in enlarged view of O_2-TPD in the range of 50 °C to 210 °C, the peaks corresponding to surface O^- and O_2^- species are observed. $NiCo_2O_4$ and $CuCo_2O_4$ exhibit the higher desorption rates and the lower desorption temperature for surface O^- and O_2^- species by
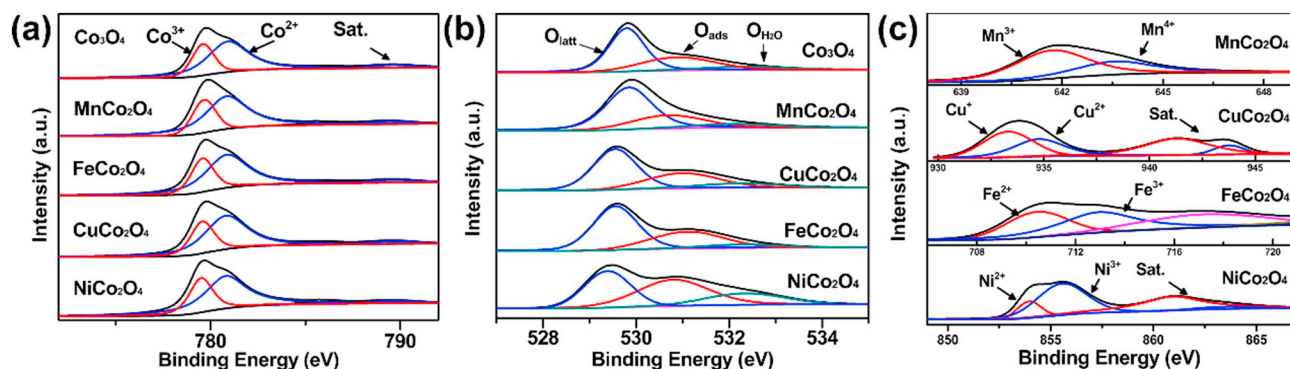
Fig. 7. Co 2p3/2 (a), O 1s (b) and second metal 2p3/2 (c) XPS spectra of the catalysts.

Table 2
Summary of oxygen storage capacity (OSC) and surface elemental components (XPS) of the catalysts.

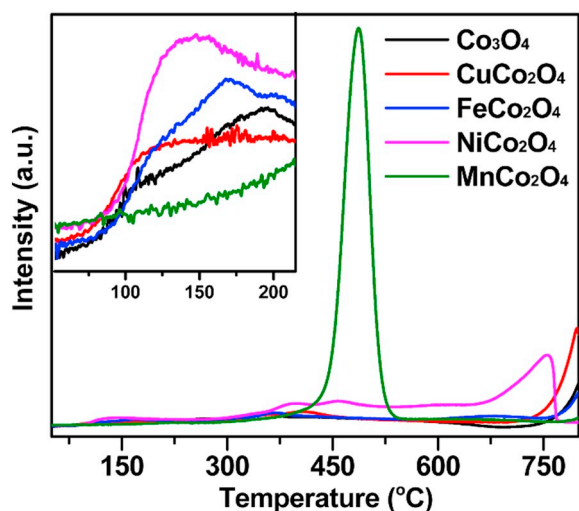| Samples	OSC (μmol/g)	Molar ratios by XPS		CO consumption (μmol)	
		Co^{3+}/Co^{2+}	O_{ads}/O_{latt}	Heat	Irradiation + Heat
Co_3O_4	863	0.5	0.5		
$MnCo_2O_4$	563	0.5	0.4		
$FeCo_2O_4$	761	0.5	0.6		
$CuCo_2O_4$	2896	0.5	0.6		
$NiCo_2O_4$	1667	0.5	1.2	14.97	19.06

Fig. 8. O_2-TPD profiles of catalysts.

comparison with $FeCo_2O_4$ and Co_3O_4. No obvious desorption peak of surface O^- and O_2^- species for $MnCo_2O_4$ is observed. Overall consideration of desorption rate, desorption temperature and desorption amount of surface O^- and O_2^- species, an approximate rank is given as the order: $NiCo_2O_4 > CuCo_2O_4 > FeCo_2O_4 > Co_3O_4 > MnCo_2O_4$. This result is the same with catalytic performance of catalysts for toluene oxidation. Therefore, to sum up, catalyst with more absorbed oxygen species and good low-temperature desorption capacity shows the better catalytic ability for toluene degradation.

3.4. Photo-thermocatalysis mechanism

Based on the results mentioned above, it is concluded that toluene oxidation on Co-based catalysts is a light-driven thermocatalytic process. The thermal energy supplement in this procedure is actually from the effective photo-thermal conversion under irradiation. Thus, the

strong light-capturing capacity is the prerequisite for the light-off temperature of toluene oxidation. Simultaneously, it is closely related to doped metal ions as well as physicochemical properties of catalyst such as surface area, active oxygen species, *etc.* As observed for $NiCo_2O_4$, it possesses strong light absorption capacity, enlarged surface area, more surface adsorbed oxygen species, and good oxygen desorption, therefore, the synergetic effect contributes to the higher catalytic activity for toluene decomposition compared to other catalysts.

Furthermore, *in situ* DRIFTS was carried out to explore the degradation pathways for toluene oxidation on $NiCo_2O_4$ under the direct electric heating condition and irradiation condition. As shown in Fig. 9, after being exposed to the toluene/N_2 vapors, there are four bands can be detected in stretching region of C−H (2850–3100 cm^{-1}) due to the adsorption of toluene [54]. The bands of 3038 and 3077 cm^{-1} can be ascribed to C−H stretching vibrational bands from aromatic rings, and others bands ascribed to C−H stretching from methylene (-CH_2) group can be observed at 2880 and 2938 cm^{-1}. Moreover, the bands originated from the vibration of aromatic ring appear at 1495 and 1605 cm^{-1}, which also verify that toluene can be easily absorbed on the surface of $NiCo_2O_4$ and the aromatic ring structure remains intactly at low temperature [54]. Upon irradiation or heating, these bands corresponding to toluene are rapidly disappeared and a series of new bands appear, indicating oxidation of toluene occurs on $NiCo_2O_4$. After heating at 230 °C for 10 min or irradiation with 400 mW/cm^2 for 30 min, both of IR spectra show similar peaks. For heating condition, an obvious new band at 1589 cm^{-1} (1597 cm^{-1} for irradiation) can be assigned to benzyl alcohol, implying the toluene is first oxidized to benzyl alcohol [54]. And the bands at 1664 cm^{-1} (both of heating and irradiation) can be ascribed to the benzaldehyde species on the catalyst [55]. The characteristic peaks of carboxylate group also appear (1350–1550 cm^{-1} for both of heating and irradiation), which is identified as the important intermediates in toluene decomposition [31,36,56]. Thus, the reaction pathway on $NiCo_2O_4$ under heating or irradiation condition can be described as follows: toluene → benzyl alcohol → benzaldehyde → benzoate species → H_2O and CO_2. It is also noted that the peak intensities of intermediates under irradiation is weaker than that of peaks at heating condition, which indicates that the intermediates can be more efficiently oxidized to final products under irradiation. This phenomenon suggests there is a slight difference existed in reaction process under heating and irradiation although both are intrinsically thermocatalysis.

As discussed above, the surface-active oxygen species on $NiCo_2O_4$ plays a key role in photo-thermocatalysis of toluene oxidation, thus CO-TPR was used to study the amount and mobility of active oxygen on $NiCo_2O_4$. Considering the slight difference in the reaction process between heating and irradiation condition, CO-TPR behavior was studied with temperature rising from room temperature to 214 °C by direct heating or irradiation with auxiliary heating. It should be referred that the surface temperature of $NiCo_2O_4$ under irradiation with auxiliary heating is faster to reach to 214 °C than that of direct heating (Fig. S8)
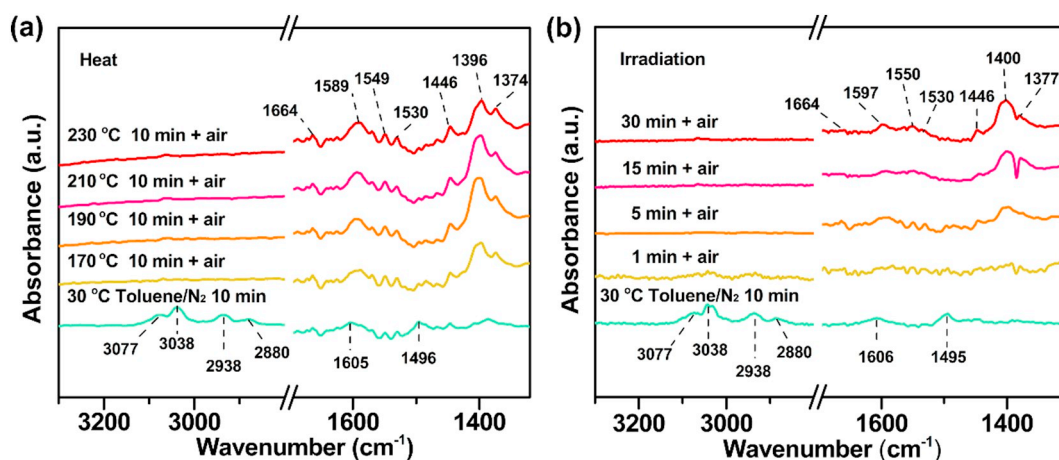
Fig. 9. *In situ* DRIFTS spectra for NiCo$_2$O$_4$ catalyst under exposure to toluene in air at different temperatures by external heating (a) and under irradiation (simulated sunlight, 400 mW/cm^2) (b).
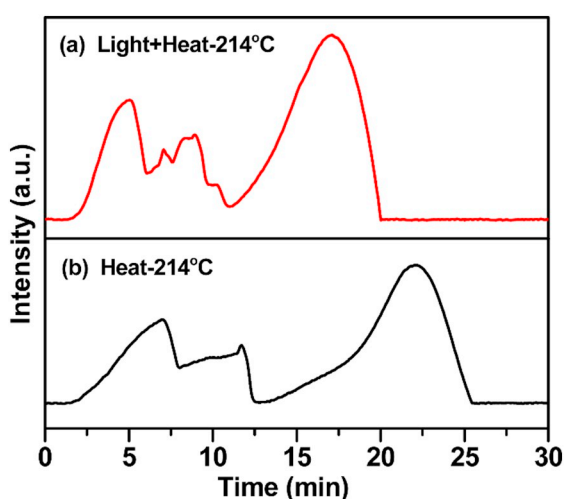

Fig. 10. CO-TPR profile of NiCo$_2$O$_4$ (from room temperature to 214 °C) under the full spectrum irradiation (100 mW/cm^2) with auxiliary heating (a) and under direct heating condition (b).

Fig. 11. Durability of NiCo$_2$O$_4$ under irradiation of 400 mW/cm^2 simulated sunlight in air stream containing 220 ppm toluene (GHSV = 32,000 mL/g·h).

with the same conditions (reactor, heating rate, gas-flow rate). As a result, CO consumption peaks of NiCo$_2$O$_4$ come out early under irradiation with auxiliary heating compared to direct heating (Fig. 10). In other words, the existence of light accelerates the release of active oxygen species to participate in CO oxidation, leading to the forward-shift of CO consumption peaks. Furthermore, it is observed that the intensity of CO consumption peaks is obviously enhanced under irradiation with auxiliary heating (Table 2), suggesting more oxygen species are activated to participate in CO oxidation. The possible explanation for the enhanced CO consumption is that the inert O species under single heating conditions was promoted to its excited state and reacted with CO molecule upon irradiation of simulated sunlight [8], leading to the enhanced consumption of CO. Thus, it can be deduced that the photo-thermocatalytic process not only boosts the release of active oxygen species but also increases the amount of active oxygen species of the catalyst due to light irradiation, which results in the improvement of catalytic activity as compared to that under pure heating condition.

3.5. Durability

The catalytic stability of NiCo$_2$O$_4$ for toluene degradation was carried out by ten reaction cycles (each cycle for 2 h). As depicted in
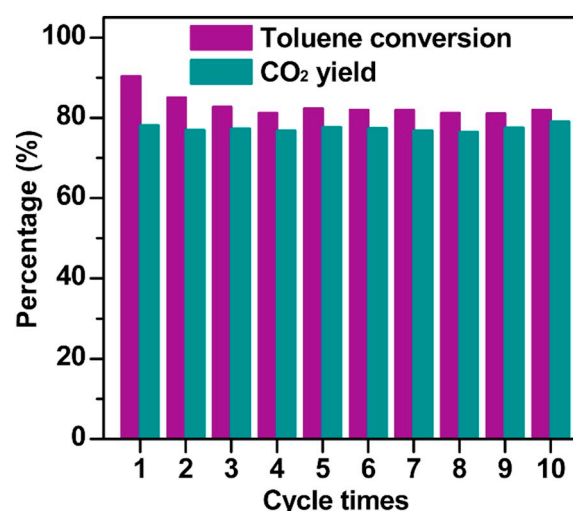
Fig. 11, after ten cycles, the toluene conversion is slightly decreased to 82% from 91%, which can be ascribed to the coverage of small amount intermediates on active sites of catalyst in reaction process. Toluene conversion is finally reached to stability owing to the establishment of a reaction equilibrium. The CO$_2$ yields for ten cycles indicate that toluene mineralization maintains a stable level at around 80%. These results suggest that NiCo$_2$O$_4$ exhibits the good catalytic stability for toluene degradation under irradiation of simulated sunlight within 20 h (each cycle for 2 h, 10 cycles).

4. Conclusions

To summarize, the ACo$_2$O$_4$ spinel catalysts have been synthesized *via* a simple co-precipitation method. The Co-based samples exhibit strong light absorption over the entire solar spectrum and efficient photo-thermal conversion, providing enough thermal energy for driving photo-thermocatalytic reactions. The NiCo$_2$O$_4$ displays efficient catalytic performance and stability (around 80% of toluene conversion and mineralization at least for 10 cycles) for toluene oxidation under illumination, which can be assigned to synergistic effect of more surface active oxygen species, strong light absorption, high photo-thermal conversion efficiency, enlarged surface area and better OCS. The addition of Ni considerably enhances the concentration of surface oxygen defects of NiCo$_2$O$_4$, leading to the increased amount of surface adsorbed

oxygen species, thereby promoting its photo-thermocatalytic activity. A photo-promotion effect was also found to be able to promote the catalytic activity: the mobility of active oxygen species in $NiCo_2O_4$ is improved under irradiation, which is in favor of toluene combustion, resulting in a higher catalytic activity under irradiation than that of pure heat. Thus, these findings in this work highlight a promising application for efficient environment purification by harvesting inexhaustible solar energy.

Acknowledgments

Appendix A. Supplementary data

Supplementary data to this article can be found online at https://doi.org/10.1016/j.apsusc.2019.04.093.

References

[1] S. Gokhale, T. Kohajda, U. Schlink, Source apportionment of human personal exposure to volatile organic compounds in homes, offices and outdoors by chemical mass balance and genetic algorithm receptor models, Sci. Total Environ. 407 (2008) 122–138.

[2] W.L. Wang, Q. Meng, Y. Xue, X. Weng, P. Sun, Z. Wu, Lanthanide perovskite catalysts for oxidation of chloroaromatics: secondary pollution and modifications, J. Catal. 366 (2018) 213–222.

[3] J. Karuppiah, E. Linga Reddy, P. Manoj Kumar Reddy, B. Ramaraju, R. Karvembu, C. Subrahmanyam, Abatement of mixture of volatile organic compounds (VOCs) in a catalytic non-thermal plasma reactor, J. Hazard. Mater. 237-238 (2012) 283–289.

[4] X. Qian, D. Yue, Z. Tian, M. Reng, Y. Zhu, M. Kan, T. Zhang, Y. Zhao, Carbon quantum dots decorated Bi_2WO_6 nanocomposite with enhanced photocatalytic oxidation activity for VOCs, Appl. Catal. B Environ. 193 (2016) 16–21.

[5] H. Tong, S. Ouyang, Y. Bi, N. Umezawa, M. Oshikiri, J. Ye, Nano-photocatalytic materials: possibilities and challenges, Adv. Mater. 24 (2012) 229–251.

[6] J. Gao, J. Miao, P.-Z. Li, W.Y. Teng, L. Yang, Y. Zhao, B. Liu, Q. Zhang, A p-type Ti (iv)-based metal-organic framework with visible-light photo-response, Chem. Commun. 50 (2014) 3786–3788.

[7] B. Sun, W. Zhou, H. Li, L. Ren, P. Qiao, F. Xiao, L. Wang, B. Jiang, H. Fu, Magnetic Fe_2O_3/mesoporous black TiO_2 hollow sphere heterojunctions with wide-spectrum response and magnetic separation, Appl. Catal. B Environ. 221 (2018) 235–242.

[8] M. Zeng, Y. Li, F. Liu, Y. Yang, M. Mao, X. Zhao, Cu doped OL-1 nanoflower: a UV–vis-infrared light-driven catalyst for gas-phase environmental purification with very high efficiency, Appl. Catal. B Environ. 200 (2017) 521–529.

[9] J.J. Li, E.Q. Yu, S.C. Cai, X. Chen, J. Chen, H.P. Jia, Y.J. Xu, Noble metal free, CeO_2/ $LaMnO_3$ hybrid achieving efficient photo-thermal catalytic decomposition of volatile organic compounds under IR light, Appl. Catal. B Environ. 240 (2019) 141–152.

[10] J.W. Kim, S.J. Lee, P. Biswas, T.I. Lee, J.M. Myoung, Solution-processed n-ZnO nanorod/p-Co_3O_4 nanoplate heterojunction light-emitting diode, Appl. Surf. Sci. 406 (2017) 192–198.

[11] L. Lan, Z. Shi, Q. Zhang, Y. Li, Y. Yang, S. Wu, X. Zhao, Defects lead to a massive enhancement in the UV-Vis-IR driven thermocatalytic activity of Co_3O_4 mesoporous nanorods, J. Mater. Chem. A 6 (2018) 7194–7205.

[12] C. Tang, E. Liu, J. Wan, X. Hu, J. Fan, Co_3O_4 nanoparticles decorated Ag_3PO_4 tetrapods as an efficient visible-light-driven heterojunction photocatalyst, Appl. Catal. B Environ. 181 (2016) 707–715.

[13] M. Roland, Semiconductor composites: strategies for enhancing charge carrier separation to improve photocatalytic activity, Adv. Funct. Mater. 24 (2014) 2421–2440.

[14] Y. Yu, T. Takei, H. Ohashi, H. He, X. Zhang, M. Haruta, Pretreatments of Co_3O_4 at moderate temperature for CO oxidation at -80°C, J. Catal. 267 (2009) 121–128.

[15] Y. Du, W. Huang, Z. Hua, Y. Wang, X. Cui, M. Wu, Z. Shu, L. Zhang, J. Wang, H. Chen, J. Shi, A facile ultrasonic process for the preparation of Co_3O_4 nanoflowers for room-temperature removal of low-concentration NOx, Catal. Commun. 57 (2014) 73–77.

[16] Z. Cheng, Z. Chen, J. Li, S. Zuo, P. Yang, Mesoporous silica-pillared clays supported nanosized Co_3O_4-CeO_2 for catalytic combustion of toluene, Appl. Surf. Sci. 459 (2018) 32–39.

[17] J.J. Li, S.C. Cai, E.Q. Yu, B. Weng, X. Chen, J. Chen, H.P. Jia, Y.J. Xu, Efficient infrared light promoted degradation of volatile organic compounds over photo-thermal responsive Pt-rGO-TiO_2 composites, Appl. Catal. B Environ. 233 (2018) 260–271.

[18] X. Chen, J.J. Li, X. Chen, S.C. Cai, E.Q. Yu, J. Chen, H.P. Jia, MOF-templated approach for hollow NiO_x/Co_3O_4 catalysts: enhanced light-driven thermocatalytic degradation of toluene, ACS Appl. Nano Mater. 1 (2018) 2971–2981.

[19] N.J. Lawrence, J.R. Brewer, L. Wang, T.S. Wu, J. Wells-Kingsbury, M.M. Ihrig, G. Wang, Y.-L. Soo, W.N. Mei, C.L. Cheung, Defect engineering in cubic cerium oxide nanostructures for catalytic oxidation, Nano Lett. 11 (2011) 2666–2671.

[20] S. Bai, N. Zhang, C. Gao, Y. Xiong, Defect engineering in photocatalytic materials, Nano Energy 53 (2018) 296–336.

[21] S.V. Kalinin, N.A. Spaldin, Functional ion defects in transition metal oxides, Science 341 (2013) 858.

[22] C. Liu, H. Xian, Z. Jiang, L. Wang, J. Zhang, L. Zheng, Y. Tan, X. Li, Insight into the improvement effect of the Ce doping into the SnO_2 catalyst for the catalytic combustion of methane, Appl. Catal. B Environ. 176-177 (2015) 542–552.

[23] J. Chen, X. Chen, W. Xu, Z. Xu, J. Chen, H.P. Jia, J. Chen, Hydrolysis driving redox reaction to synthesize Mn-Fe binary oxides as highly active catalysts for the removal of toluene, Chem. Eng. J. 330 (2017) 281–293.

[24] R. Wang, S. Ni, G. Liu, X. Xu, Hollow CaTiO$_3$ cubes modified by La/Cr co-doping for efficient photocatalytic hydrogen production, Appl. Catal. B Environ. 225 (2018) 139–147.

[25] J. Li, S. Xiong, Y. Liu, Z. Ju, Y. Qian, High electrochemical performance of monodisperse $NiCo_2O_4$ mesoporous microspheres as an anode material for Li-ion batteries, ACS Appl. Mater. Inter. 5 (2013) 981–988.

[26] A. Pendashteh, S.E. Moosavifard, M.S. Rahmanifar, Y. Wang, M.F. El-Kady, R.B. Kaner, M.F. Mousavi, Highly ordered mesoporous $CuCo_2O_4$ nanowires, a promising solution for high-performance supercapacitors, Chem. Mater. 27 (2015) 3919–3926.

[27] B. Zhu, S. Tang, S. Vongehr, H. Xie, X. Meng, Hierarchically MnO_2-nanosheet covered submicrometer-$FeCo_2O_4$-tube forest as binder-free electrodes for high energy density all-solid-state supercapacitors, ACS Appl. Mater. Inter. 8 (2016) 4762–4770.

[28] A.K. Mondal, D. Su, S. Chen, A. Ung, H.S. Kim, G. Wang, Mesoporous $MnCo_2O_4$ with a flake-like structure as advanced electrode materials for lithium-ion batteries and supercapacitors, Chemistry 21 (2015) 1526–1532.

[29] R. Peng, X. Sun, S. Li, L. Chen, M. Fu, J. Wu, D. Ye, Shape effect of Pt/CeO_2 catalysts on the catalytic oxidation of toluene, Chem. Eng. J. 306 (2016) 1234–1246.

[30] A. Jayakumar, R.P. Antony, R. Wang, J.M. Lee, MOF-derived hollow cage $Ni_xCo_{3-x}O_4$ and their synergy with graphene for outstanding supercapacitors, Small 13 (2017).

[31] X. Wang, Y. Liu, T. Zhang, Y. Luo, Z. Lan, K. Zhang, J. Zuo, L. Jiang, R. Wang, Geometrical-site-dependent catalytic activity of ordered mesoporous Co-based spinel for benzene oxidation: in situ DRIFTS study coupled with Raman and XAFS spectroscopy, ACS Catal. 7 (2017) 1626–1636.

[32] S. Zhao, F. Hu, J. Li, Hierarchical core–shell Al_2O_3@Pd-CoAlO microspheres for low-temperature toluene combustion, ACS Catal. 6 (2016) 3433–3441.

[33] J. López-Sánchez, A. Serrano, A. Del Campo, M. Abuín, O. Rodríguez de la Fuente, N. Carmona, Sol–gel synthesis and micro-Raman characterization of ε-Fe_2O_3 micro- and nanoparticles, Chem. Mater. 28 (2016) 511–518.

[34] C. Liu, H. Sun, J. Qian, Z. Chen, F. Chen, S. Liu, Y. Lv, X. Lu, A. Chen, Ultrafine Mn_3O_4/CeO_2 nanorods grown on reduced graphene oxide sheets as high-performance supercapacitor electrodes, J. Alloy. Compd. 722 (2017) 54–59.

[35] J. Chen, Z. He, G. Li, T. An, H. Shi, Y. Li, Visible-light-enhanced photo-thermocatalytic activity of ABO_3-type perovskites for the decontamination of gaseous styrene, Appl. Catal. B Environ. 209 (2017) 146–154.

[36] X. Chen, X. Chen, S.C. Cai, J. Chen, W.J. Xu, H.P. Jia, J. Chen, Catalytic combustion of toluene over mesoporous Cr_2O_3-supported platinum catalysts prepared by in situ pyrolysis of MOFs, Chem. Eng. J. 334 (2018) 768–779.

[37] B. Choudhury, M. Dey, A. Choudhury, Defect generation, d-d transition, and band gap reduction in Cu-doped TiO_2 nanoparticles, Inter. Nano Lett. 3 (2013) 25.

[38] J. Chen, Y. Li, S. Fang, Y. Yang, X. Zhao, UV–vis-infrared light-driven thermo-catalytic abatement of benzene on Fe doped OMS-2 nanorods enhanced by a novel photoactivation, Chem. Eng. J. 332 (2018) 205–215.

[39] H.S. Park, C.Y. Lee, E. Reisner, Photoelectrochemical reduction of aqueous protons with a CuO|$CuBi_2O_4$ heterojunction under visible light irradiation, Phys. Chem. Chem. Phys. 16 (2014) 22462–22465.

[40] W. Wang, J. Xu, Structure and visible light luminescence of 3D flower-like Co_3O_4 hierarchical microstructures assembled by hexagonal porous nanoplates, ACS Appl. Mater. Inter. 7 (2015) 415–421.

[41] J. Zhao, J. Nan, Z. Zhao, N. Li, J. Liu, F. Cui, Energy-efficient fabrication of a novel multivalence Mn_3O_4-MnO_2 heterojunction for dye degradation under visible light irradiation, Appl. Catal. B Environ. 202 (2017) 509–517.

[42] A. Duret, M. Grätzel, Visible light-induced water oxidation on mesoscopic α-Fe_2O_3 films made by ultrasonic spray pyrolysis, J. Phys. Chem. B 109 (2005) 17184–17191.

[43] Z. Zhang, C. Shao, X. Li, C. Wang, M. Zhang, Y. Liu, Electrospun nanofibers of p-type NiO/n-type ZnO heterojunctions with enhanced photocatalytic activity, ACS Appl. Mater. Inter. 2 (2010) 2915–2923.

[44] M.A. Lockwood, K. Wang, J.M. Mayer, Oxidation of toluene by [(phen)$_2$Mn(μ-O)$_2$Mn(phen)$_2$]$^{4+}$ via initial hydride abstraction, J. Am. Chem. Soc. 121 (1999) 11894–11895.

[45] X. Huang, I.H. El-Sayed, W. Qian, M.A. El-Sayed, Cancer cell imaging and photothermal therapy in the near-infrared region by using gold nanorods, J. Am. Chem. Soc. 128 (2006) 2115–2120.

[46] S. Mo, S. Li, J. Li, Y. Deng, S. Peng, J. Chen, Y. Chen, Rich surface Co(iii) ions-enhanced Co nanocatalyst benzene/toluene oxidation performance derived from $Co^{II}Co^{III}$ layered double hydroxide, Nanoscale 8 (2016) 15763–15773.

[47] J.-H. Zhong, A.-L. Wang, G.-R. Li, J.-W. Wang, Y.-N. Ou, Y.-X. Tong, Co_3O_4/Ni(OH)$_2$

composite mesoporous nanosheet networks as a promising electrode for super-capacitor applications, J. Mater. Chem. 22 (2012) 5656–5665.

[48] Z. Cuo, Y. Deng, W. Li, S. Peng, F. Zhao, H. Liu, Y. Chen, Monolithic Mn/Ce-based catalyst of fibrous ceramic membrane for complete oxidation of benzene, Appl. Surf. Sci. 456 (2018) 594–601.

[49] Y.P. Wang, L. Zhou, M.F. Zhang, X.Y. Chen, J.-M. Liu, Z.G. Liu, Room-temperature saturated ferroelectric polarization in BiFeO₃ ceramics synthesized by rapid liquid phase sintering, Appl. Phys. Lett. 84 (2004) 1731–1733.

[50] B. Solsona, T. García, R. Sanchis, M.D. Soriano, M. Moreno, E. Rodríguez-Castellón, S. Agouram, A. Dejoz, J.M. López Nieto, Total oxidation of VOCs on mesoporous iron oxide catalysts: soft chemistry route versus hard template method, Chem. Eng. J. 290 (2016) 273–281.

[51] M. Mao, Y. Li, J. Hou, M. Zeng, X. Zhao, Extremely efficient full solar spectrum light driven thermocatalytic activity for the oxidation of VOCs on OMS-2 nanorod

catalyst, Appl. Catal. B Environ. 174-175 (2015) 496–503.

[52] A. Bielański, J. Haber, Oxygen in catalysis on transition metal oxides, Catal. Rev. 19 (1979) 1–41.

[53] Y. Zheng, W. Wang, D. Jiang, L. Zhang, X. Li, Z. Wang, Ultrathin mesoporous Co₃O₄ nanosheets with excellent photo − /thermo-catalytic activity, J. Mater. Chem. A 4 (2016) 105–112.

[54] Z. Jia, X. Wang, F. Thevenet, A. Rousseau, Dynamic probing of plasma-catalytic surface processes: oxidation of toluene on CeO₂, Plasma Process. Polym. 14 (2017).

[55] H. Sun, Z. Liu, S. Chen, X. Quan, The role of lattice oxygen on the activity and selectivity of the OMS-2 catalyst for the total oxidation of toluene, Chem. Eng. J. 270 (2015) 58–65.

[56] Z. Zhu, F. Liu, W. Zhang, Fabricate and characterization of Ag/BaAl₂O₄ and its photocatalytic performance towards oxidation of gaseous toluene studied by FTIR spectroscopy, Mater. Res. Bull. 64 (2015) 68–75.